NJC
New Journal of Chemistry
A journal for new directions in chemistry

Accepted Manuscript

This article can be cited before page numbers have been issued, to do this please use: C. Li, W. Fang, S. Yang, Y. ZHANG, L. Zou, F. Zhou and R. Chi, *New J. Chem.*, 2025, DOI: 10.1039/D5NJ01601K.

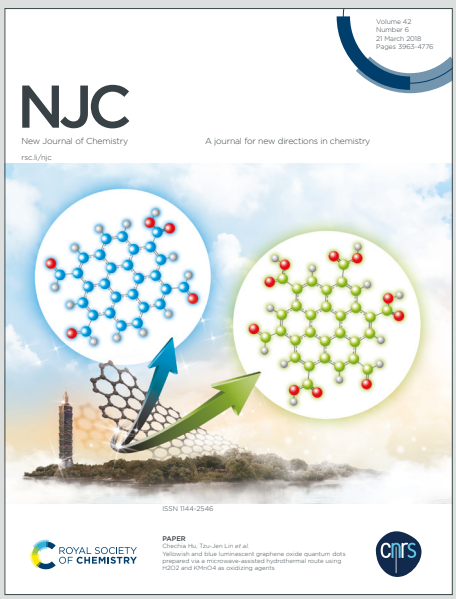

This is an Accepted Manuscript, which has been through the Royal Society of Chemistry peer review process and has been accepted for publication.

Accepted Manuscripts are published online shortly after acceptance, before technical editing, formatting and proof reading. Using this free service, authors can make their results available to the community, in citable form, before we publish the edited article. We will replace this Accepted Manuscript with the edited and formatted Advance Article as soon as it is available.

You can find more information about Accepted Manuscripts in the Information for Authors.

Please note that technical editing may introduce minor changes to the text and/or graphics, which may alter content. The journal's standard Terms & Conditions and the Ethical guidelines still apply. In no event shall the Royal Society of Chemistry be held responsible for any errors or omissions in this Accepted Manuscript or any consequences arising from the use of any information it contains.

The investigation of ion association characteristics in lanthanum acetate solution by the density functional theory and molecular dynamics simulations

Caocheng Li[a,b], Wen Fang[b], Si Yang[b], Yuefei Zhang[a,b], Lian Zou[c], Fang Zhou[a,d], Ruan Chi[a,d]

[a] Key Laboratory for Green Chemical Process of Ministry of Education, Wuhan Institute of Technology, Wuhan 430205, China

[b] School of Chemistry and Environmental Engineering, Wuhan Institute of Technology, Wuhan 430205, China

[c] School of Electronic Information, Wuhan University, Wuhan 430072, China

[d] School of Xingfa Mining Engineering, Wuhan Institute of Technology, Wuhan 430073, China

Correspondence authors: Yuefei Zhang, Fang Zhou

E-mail of correspondence authors: yuefeiz@wit.edu.cn, fzhou@wit.edu.cn

Abstract: This study investigates the structure and evolution of lanthanum acetate hydrated clusters using density functional theory (DFT) and molecular dynamics (MD) simulations to explore the influence of organic ammonium leaching agents on rare earth hydrated clusters at the microscopic level. Structural optimization, electrostatic potential (ESP) maps, and binding energies were calculated for $La(CH_3COO)_3 \bullet nH_2O$ (n=0–5) in the gas phase, and for $La(CH_3COO)_3 \bullet nH_2O$ (n=2–5) hydrated clusters using the PCM solvent model, all at the PBE0/6-311+G(d,p) level. Theoretical and experimental Raman spectra of lanthanum acetate were compared, which facilitated the determination of the hydrated cluster structure of lanthanum acetate. The findings revealed that the first hydration layer of the La acetate cluster reaches saturation when the number of water molecules is three, with the $La(CH_3COO)_3 \bullet 3H_2O$ cluster showing the lowest binding energy, indicating a stable structure. The results provide valuable insights into the structural characteristics and binding interactions within lanthanum acetate hydrated clusters, contributing to a better understanding of their behavior in solution.

Keywords: weathered crust elution-deposited rare earth ore; Lanthanum acetate clusters; Density Functional Theory; Molecular Dynamics

View Article Online
DOI: 10.1039/D5NJ01601K

1. Introduction

Rare earth is an important support for the manufacture of new materials and a key resource for the development of cutting-edge national defense technology[1, 2]. The rare earth elements in weathered crust elution-deposited rare earth ore are mainly in the form of hydration or hydroxy-hydration ions in weathering crust clay minerals, so the conventional physical mineral processing method can not be used to enrich and recover rare earth[3, 4]. At present, leaching technology is mainly used in the mining of this type of rare earths, and in the leaching process of rare earths, the rare earths in minerals are mainly leached out using neutral salts with greater cationic activity than rare earth ions[5]. Most of the actual production uses ammonium sulfate as leaching agent, but there are still problems that need to be solved such as high impurity content, water absorption and swelling of clay minerals in the leaching process, causing landslides. So many researchers have studied the process of using compound ammonium salts as leaching agents[6, 7]. A novel leaching agent combining ammonium sulfate and ammonium formate was investigated[8]. Results showed that ammonium formate enhanced rare earth mass transfer while inhibiting aluminum mass transfer. Key factors, including leaching agent pH, temperature, and liquid/solid ratio, were optimized. The best conditions for leaching rare earth and aluminum were 0.1 mol/L ammonium sulfate with 0.032 mol/L ammonium formate, pH 4–8, and room temperature. A study on rare earth leaching explored the effects of ammonium chloride mixed with ammonium acetate, tartrate, and citrate[9]. The optimal concentrations were 0.04 mol/L ammonium acetate, 0.07 mol/L ammonium tartrate, and 0.005 mol/L ammonium citrate. At pH 4, the solution of 0.2 mol/L ammonium chloride and 0.04 mol/L ammonium acetate achieved a rare earth extraction rate of 90.08%, with aluminum leaching at 26.37% and clay swelling at 2.705%. Additionally, the effects of ammonium acetate concentration and leaching temperature on the permeation process for weathered crust elution-deposited rare earth ores were investigated. However, most studies focus primarily on the experimental phenomena and results, with limited exploration of the underlying leaching mechanism of carboxylic acid-based agents.

Many studies have shown that metal ions in solution can form hydrated clusters, and solvation effects involve a combination of electrostatic interactions, dipole-dipole interactions, hydrogen bonding, induced dipole interactions, and dispersion forces[10, 11]. Mg^{2+} ion association and hydration dynamics in $MgSO_4$ solutions have been investigated using DFT and molecular dynamics[12]. Contact-associated (CA) and solvent-separated (SS) ion structures dominate, influencing crystallization and gelation. CA structures are stable but aggregate slowly,

contributing to gel formation. SS structures show active ion exchange and aggregation, promoting nucleation in supersaturated solutions. These findings clarify $MgSO_4$ nucleation mechanisms and the role of hydration dynamics.

The specific types and strengths of interactions depend on the nature of the solute and solvent molecules involved[13]. Therefore, the structure of rare earth hydrated clusters at the microscopic level is important for exploring the process of leaching rare earths and can provide a theoretical basis for efficient extraction of rare earths. Zou group used density functional theory to explore the adsorption of hydrated Pr^{3+}, Mg^{2+}, and NH_4^+ ions on the montmorillonite (001) surface[14]. Pr^{3+} exhibited the strongest adsorption energy (−1182 kJ/mol) via hydrogen bonding, surpassing Mg^{2+} (−206 kJ/mol) and NH_4^+ (−188 kJ/mol). Desorption experiments showed Pr^{3+} recovery rates of 80% with Mg^{2+} (38 mmol/L) and 65% with NH_4^+, supporting theoretical predictions and highlighting the need for higher Mg^{2+} and NH_4^+ concentrations in leaching processes.

Most of the existing studies on the leaching process of weathered crust elution-deposited rare earth ores focus on the apparent process of rare earth leaching, and there is still a lack of in-depth understanding of the solvation between organic anions and rare earth ions during the leaching process of rare earths. Therefore, revealing the structure and evolution law of ammonium acetate affecting rare earth hydration clusters at the molecular level will be a theoretical guide to study the exchange and migration mechanism of rare earth ions and develop new leaching agents.

2. Experimental and computational methods

2.1 Raman spectra analysis

Hydrated lanthanum acetate ($La(CH_3COO)_3 \cdot H_2O$, 99.9%) was procured from Shanghai Aladdin Biochemical Technology Co.,Ltd. A 0.8827 g sample was dissolved in 5 mL of deionized water to prepare a 0.5316 mol/L solution. Raman spectra of both solid and the solution phases were recorded. For the solid sample, the powder was placed on a glass slide. Measurements were performed using a HORIBA JY LabRAM HR Evolution Raman Spectrometer with a 532 nm laser, covering a spectral range of 4000-50 cm^{-1}.

View Article Online
DOI: 10.1039/D5NJ01601K

2.2 Structure optimization of hydrated clusters

The La hydrated clusters with acetate ion were investigated using DFT. The structures of the hydrated clusters of $La(CH_3COO)_3 \cdot nH_2O$ (n=0~5) were optimized at the PBE0/6-311+G(d, p) level, and the vibrational frequencies and free energies of the clusters were calculated at the same level, where the pseudopotential basis set SDD was used for La and the all-electron basis set 6-311+G(d, p) was used for non-metallic elements. For comparison, additional calculations employing the BP86 and M06-L functionals with the identical basis sets were conducted to assess the impact of the exchange-correlation functional on the structural, electronic, and energetics properties. The above work was done using the Gaussian 16 software package[15]. After optimizing the structures, changes in bond lengths and angles between the La ion and ligands in hydrated clusters of $La(CH_3COO)_3 \cdot nH_2O$ (n=0~5) were analyzed and compared.

The solvent effect on clusters is crucial, as understanding solvent influence on cluster properties aids in uncovering the microscopic mechanism of cluster formation. The polarizable continuum model (PCM)[16], a widely used implicit solvent model, represents solvent molecules as a continuous, isotropic medium. In this study, lanthanum acetate clusters optimized in the gas phase were re-optimized within the PCM solvent model and analyzed, with their properties compared to those of the gas-phase clusters. The solvent effects were further examined using the PBE0, BP86, and M06-L functionals to assess the consistency of trends in solvation energies and structural changes across different levels of theory.

2.3 Surface electrostatic potential of hydrated clusters

The work done to move a positive charge from an infinite distance to a point in space around a molecule is the electrostatic potential at that point. In the electrostatic potential diagram, red indicates the positive potential region and blue indicates the negative potential region.

In this paper, the general interaction properties function (GIPF) of the lanthanum acetate cluster is also analyzed based on the molecular surface electrostatic potential (ESP)[17]. Π denotes the average deviation of the ESP, which is viewed as an indicator of internal charge separation and can characterize the degree of surface charge separation. σ_{tot}^2、σ_+^2、σ_-^2 are the total variance of the ESP, the variance of the positive and negative portions, respectively. ν denotes the charge balance degree. When σ_+^2 equals to σ_-^2, ν attains its maximum value of 0.250. The closer the ν is to 0.250, the more possible that the molecule can interact to others through the positive and negative regions with similar extent. The product of σ_{tot}^2 and ν provides insights into the

interplay between charge homogeneity and electrostatic heterogeneity. A large value of $\nu\sigma_{tot}^2$ indicates a molecule with a strong propensity to engage in electrostatic interactions with others of its kind.[18].

2.4 The distribution and localization of electron density in clusters

Localized Orbital Locator (LOL) maps are a tool used in quantum chemistry to visualize and analyze the distribution and localization of electron density in molecules[19]. The LOL is defined as a function of the electron density ρ(r) and kinetic energy density τ(r)[20]. Once the LOL is calculated at various points in space, it can be visualized as a 2D scalar field or as contour plots (LOL maps). These maps show regions of high and low electron localization.

Weak interactions are often associated with charge transfer, and plotting the electron density difference between complexes and constituent monomers provides a common and intuitive method for studying these charge changes[21, 22]. In this paper, the electron density difference of the $La(CH_3COO)_3 \cdot 5H_2O$ cluster is calculated by subtracting the electron density of the individual fragments from the electron density of the entire cluster.

2.5 Topology analysis for electron density of hydrated clusters (AIM analysis)

Atoms in molecules (AIM) is based on the topological nature of the electron density scalar field to describe bonding in molecules.[23] When the Laplace value of $\nabla^2\rho$ at the bond critical point is negative, it means that a covalent bond is formed, and when it is positive, it means that the bond formed may be an ionic bond, a hydrogen bond, or a van der Waals interaction[24]. Positive values of the electron energy density H indicate electrostatic interactions between atoms, while negative values indicate partial covalent interactions between atoms. A higher value of electron density ρ indicates a stronger chemical bond.

2.6 Noncovalent Interaction in the hydrated clusters

The reduced density gradient(RDG) function and $sign(\lambda_2)\rho$ are a pair of very important functions for revealing weak interaction regions, and they are commonly used together in noncovalent interaction (NCI) method[25]. The RDG isosurface provides a visual representation of the regions, types, and intensities of weak interactions in molecular clusters[26]. In RDG scatter

plots and isosurface plots, blue indicates regions of strong interaction, green corresponds to weak van der Waals interaction regions, and red highlights areas of steric hindrance.

The average NCI (aNCI) method can be used to analyze the molecular dynamics trajectories. Unlike the original NCI method, where the electron density and its gradient norm $|\nabla\rho|$ are calculated for a single geometry, aNCI computes these values across multiple frames in a trajectory file and then averages them (denoted $\overline{\rho}$ and $\overline{\nabla\rho}$)[27]. In the aNCI diagram, blue indicates strong interaction regions, green represents van der Waals interaction regions, and red highlights areas of steric hindrance region.

aNCI method also defines a new quantity named thermal fluctuation index (TFI) to reveal the stability of weak interaction[28]

$$\mathrm{TFI}(\mathrm{r}) = \frac{std[\rho(\mathrm{r})]}{\overline{\rho(\mathrm{r})}} \qquad (1)$$

whose numerator is standard deviation of electron density in the dynamical trajectory, which can be calculated as

$$std[\rho(\mathrm{r})] = \sqrt{\frac{\sum_i \left[\rho_i(\mathrm{r}) - \overline{\rho(\mathrm{r})}\right]^2}{n}} \qquad (2)$$

Where n is the number of frames considered, and ρ_i is the electron density calculated based on the geometry of frame *i*. By mapping the TFI onto the aRDG isosurface, the stability of each weak interaction region can be visually assessed through color variations. In the TFI chart, colored by the heat wave index, blue represents regions of stable interaction, green indicates regions with relatively lower interaction stability, and red highlights regions of unstable interaction in the aNCI analysis.

The ESP, GIPF values, LOL, electron density difference, TFI maps, RDG and aRDG were conducted using the Multiwfn 3.8 software package[29], with RDG visualization accomplished using the Visual Molecular Dynamics (VMD) software package.[30]

2.7 Binding and Hydration Energies of Lanthanum Acetate Hydrated Clusters

Binding energy is typically calculated as the difference between the energy of the complex and the sum of the energies of the individual fragments that compose it. Binding energy serves as an indicator of system stability: the smaller the binding energy, the more stable the structure.[31] The binding energy ($\Delta E_{binding}$) is calculated using the formula:

$$\Delta E_{binding} = E(AB) - [E(A) + E(B)] \qquad (3)$$

where E(AB) represents the energy of the complex, and E(A) and E(B) are the energies of fragments A and B, respectively.

In this study, the stability of various clusters was compared and the trend of their binding energy was analyzed. If Gibbs free energies of reaction are required, the binding energy can be calculated as the sum of electronic and thermal free energies (*G*) at 298.15 K and 1 atm.

The hydration energy of a cluster ($\Delta G_{hydration}$) is the change in energy that occurs when a cluster in a gas is dissolved in water. In this paper, $\Delta G_{hydration}$ is calculated by the difference of the sum of electron free energy and thermal free energy (G_{water}) in water and gas phase electron free energy and thermal free energy (G_{gas}).

$$\Delta G_{hydration}=G_{water}-G_{gas} \quad (4)$$

2.8 The molecular dynamics simulation of lanthanum acetate solution

To study the real-time dynamics of hydrated clusters over nanoseconds, molecular dynamics simulations of lanthanum acetate solutions were conducted at different temperatures (275 K, 300 K and 325 K) and concentrations (0.1329 mol/L, 0.5316 mol/L and 0.9302 mol/L) in a 5 nm cube box. The SPC/E model was employed to represent the water molecules. The entire molecular dynamics simulation was carried out using the GAFF force field. Bonds and angles parameters based on Cartesian Hessian matrix were calculated with Gaussian 16 software[15], while the GAFF parameters for La^{3+} and CH_3COO^- were generated using Sobtop code[32]. Energy minimization was first performed for 200 ps using the conjugate gradient (CG) method to optimize the system's initial configuration to eliminate the severely unreasonable contacts in the model. Subsequently, a kinetic simulation with a time step of 2 fs was conducted under the isothermal-isobaric (NPT) ensemble for a total simulation time of 5 ns to generate data and trajectories. The leap frog method was used for dynamics, and the Particle-mesh Ewald (PME) method with a 1.0 nm cutoff was applied for the electrostatic interaction. Temperature control was managed using the velocity-rescale method, and pressure (1 atm) was maintained using the Parrinello-Rahman method. Subsequent analysis was carried out using GROMACS[33] and VMD software packages[30].

The RDF (*g(r)*) describes the distribution characteristics of particles at a distance *r* from a reference particle in a system, and its calculation is based on statistical analysis of the spatial coordinates of particles[34]. The specific steps are as follows: taking each particle in the system as a reference point, count the average number of target particles <*N(r, dr)*> within the spherical

shell from r to $r+dr$ away from it; then, combined with the volume of the spherical shell $4\pi r^2 dr$ and the average number density of the system $\rho_0=N/V$ (where N is the total number of particles and V is the system volume), $g(r)$ is calculated using the formula:

$$g(r) = \frac{\langle N(r, dr) \rangle}{4\pi r^2 dr \cdot \rho_0} \qquad (5)$$

In the formula, the numerator represents the average number of particles in the spherical shell, and the denominator is the theoretical number of particles in that spherical shell under a uniform distribution ($4\pi r^2 dr \cdot \rho_0$). Therefore, $g(r)$ is essentially the ratio of the actual particle number density to the average density, which can intuitively reflect the degree of aggregation or sparseness of particles at a specific distance. During calculation, it is necessary to eliminate periodic boundary effects, average data from multiple trajectory frames to improve reliability, and perform smoothing to highlight characteristic peaks (such as the distance peak corresponding to coordination bonds).

The coordination number (CN) refers to the total number of target particles within a specific distance range (usually the first coordination shell, corresponding to the interval of the main peak of the RDF) around the reference particle. The formula for calculating the coordination number using the RDF is $CN=4\ \pi\ \rho\ \int r^2 g(r)dr$, By integrating the above expression within the coordination range, the actual number of target particles within the coordination shell can be cumulatively obtained, thereby determining the coordination number.

3 Results and Discussion

3.1 The Choice of DFT Functional

The computational results reveal significant variations in the predicted properties of $La(CH_3COO)_3 \cdot 3H_2O$ cluster depending on the choice of density functional theory (DFT) method. Among the three functionals employed - PBE0, BP86, and M06-L - systematic differences emerge in their predictions of bond lengths, electron density characteristics, and energetics. In the gas phase, BP86 and M06-L yield average La-O bond lengths of 2.6040 Å and 2.6117 Å, respectively, exceeding the PBE0 result (2.5861 Å) by 0.0178-0.0256 Å. Notably, the PBE0-derived bond lengths exhibit superior agreement with the experimental value of 2.5589 Å, obtained from single-crystal XRD analysis of hydrated lanthanum lactate (Molecules 2023, 28,

5896), whereas BP86 and M06-L systematically overestimate these distances. This strong alignment between PBE0 calculations and experimental data underscores the validity of our methodological approach. The suitability of PBE0 for lanthanide complexes is further supported by its successful application in prior studies of analogous systems, including investigations of Pr complexes using SDD pseudopotentials [35]. A detailed comparison of the computational methods and results is provided in Table S1 (Supplementary Materials). Given these findings, we adopt the PBE0 functional for all subsequent calculations.

3.2 Structural optimization of lanthanum acetate hydrated clusters

The stability of hydrated clusters is significantly influenced by the number of water molecules present. In lanthanum acetate systems, the first hydration shell exclusively comprises water molecules directly coordinated to the lanthanum center, whereas the total coordination number incorporates both these waters and oxygen atoms from acetate ligands. To investigate the structural characteristics of the first hydration layer in lanthanum acetate, we optimized $La(CH_3COO)_3 \bullet nH_2O$ (n=0~5) cluster geometries at the PBE0 /6-311+G(d, p) level, followed by frequency calculation at the same theoretical level. The resulting optimized structures are presented in **Figure 1**.

Figure 1 shows that water molecules closely surround the lanthanum ion and directly interact with it. As the number of water molecules increases, the first hydration layer approaches saturation, with three water molecules directly interacting with the lanthanum ion. Beginning with the fourth water molecule, the water molecules no longer interact directly with the lanthanum ions but instead interact with the oxygen in the acetate ions.

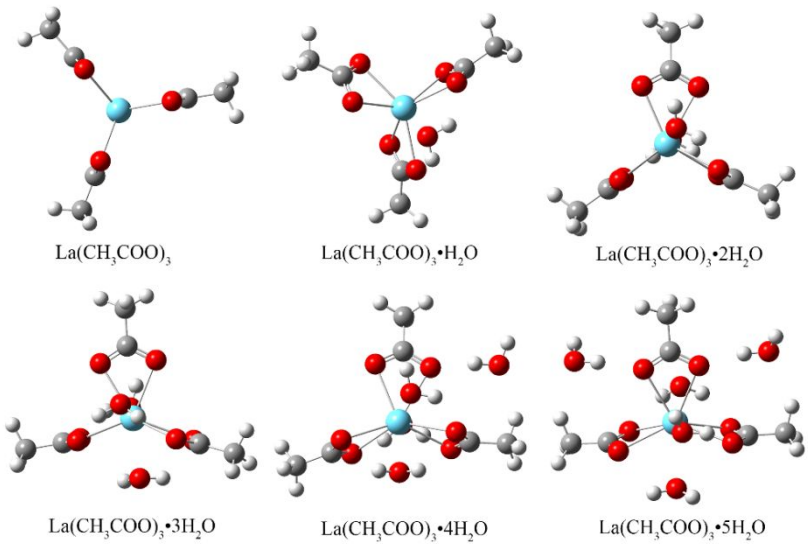

Figure 1 The structures of $[La(CH_3COO^-)_3 \cdot (H_2O)_n]^+$ (n=0~5) clusters optimized at

PBE0/6-311+G(d,p) level in gas. Blue, red and white balls denote lanthanum, oxygen and hydrogen atoms, respectively.

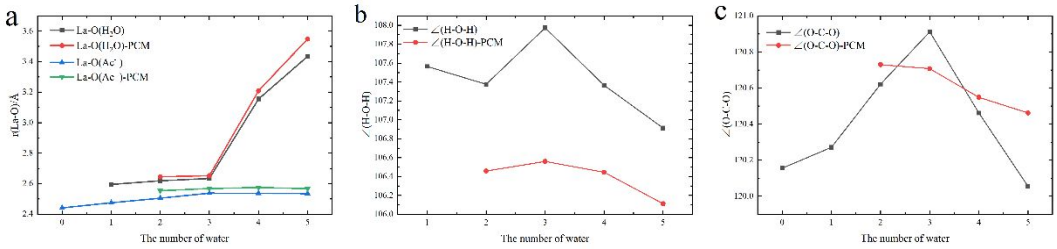

Figure 2 Bond lengths of lanthanum to oxygen of ligands and bond angles in ligands (bond lengths in Å and bond angles in degrees) (a) r(La-O_{H2O}) and r(La-O_{Ac}^-) in gas phase and PCM; (b) ∠(H-O-H) in gas phase and PCM; (c) ∠(O-C-O) in gas phase and PCM

Figure 2 presents the bond lengths between lanthanum and the acetate ligand, as well as the bond angles of the ligand, after the formation of a stable lanthanum acetate hydrated cluster. It can be observed that the distance r(La-O_{H2O}) between lanthanum and water is generally larger than the distance r(La-O_{Ac-}) between lanthanum and acetate. As the number of water molecules increases, the average coordination bond length between lanthanum and oxygen in water increases. Furthermore, when the number of water molecules reaches four, there is a significant increase in the average distance between lanthanum and oxygen in water. This is because, at this point, water molecules no longer directly coordinate with lanthanum ion. Instead, the hydrogen atoms in water interacts with acetate ions, forming hydrogen bonds. When the number of water molecules ranges from 0 to 3, the average coordination bond length between lanthanum and oxygen in acetate slightly increases. However, as the number of water molecules increases from 3 to 5, the bond length tends to stabilize. This suggests that lanthanum has a stronger tendency to coordinate with the oxygen in acetate. In the PCM solvent model, the distance between lanthanum and the ligand is slightly greater than in the gas phase.

The average bond angles of the water molecules in the lanthanum acetate hydrated cluster increased relative to the initial value of 104.5°. The largest deformation in the average bond angle occurs in the $La(CH_3COO)_3•3H_2O$ cluster, which, according to the optimized structure analysis, is due to the higher symmetry of this cluster. In contrast, the $La(CH_3COO)_3•5H_2O$ cluster shows the smallest average bond angle deformation. This is because the addition of water molecules increases the distance between the water molecules and the central lanthanum ion, reducing the influence of lanthanum on the water molecules.

View Article Online
DOI: 10.1039/D5NJ01601K

3.3 Comparison of theoretical and experimental Raman spectra

In this paper, the theoretical Raman spectra of $La(CH_3COO)_3 \cdot nH_2O$ (n=0~5) in the gas phase and $La(CH_3COO)_3 \cdot nH_2O$ (n=2~5) in the Polarizable Continuum Model (PCM) solvent model were calculated using density functional theory (DFT). Concurrently, experimental Raman spectra of solid lanthanum acetate ($La(CH_3COO)_3 \cdot H_2O$) and aqueous lanthanum acetate solutions were measured to validate the theoretical predictions.

By comparing the theoretical Raman spectra of the hydrated clusters (as shown in **Figure 3**), it is evident that as the number of water molecules increases, the intensity of bands in Band 1 (3000–3600 cm^{-1}) also increases. These bands are attributed entirely to the O-H stretching vibrations of water molecules, which exhibit stronger hydrogen bonding interactions in larger hydration shells. The experimental spectra also show a prominent vibrational peak in Band 1, with the solution spectrum displaying a broad, asymmetric profile due to the dynamic hydrogen-bonding network of water in the liquid phase, as opposed to the more structured environment in the solid state.

The weak Band 2 (~1630 cm^{-1}) corresponds to the scissoring bending vibration (δ H-O-H) of water molecules. This peak is more pronounced in the PCM model, where explicit solvation effects are accounted for, and its intensity increases significantly with the number of water molecules in the cluster. In the experimental measurements, Band 2 is broader and more intense in the solution sample compared to the solid sample, reflecting the greater mobility and disorder of water molecules in the liquid phase.

Bands 3–5 (1300–1500 cm^{-1}) correspond to the out-of-plane bending vibrations (γ C-H) of the acetate ions. In the PCM model, Band 4 (~1420 cm^{-1}) splits into two distinct peaks, a phenomenon that is also observed in the experimental spectra of both the solution and solid samples. However, this splitting is absent in the gas-phase model, suggesting that solvent interactions play a crucial role in modulating the vibrational modes of the acetate group.

Band 6 (~930 cm^{-1}) corresponds to the C-C stretching vibration (ν C-C) of the acetate ion, while Band 7 (~680 cm^{-1}) arises from the scissoring bending vibration (δ O-C-O) of the carboxylate group. These peaks are minimally affected by solvation and show excellent agreement between theoretical and experimental spectra, confirming their assignment as internal modes of the acetate ion rather than solvent-coupled vibrations [36].

View Article Online
DOI: 10.1039/D5NJ01601K

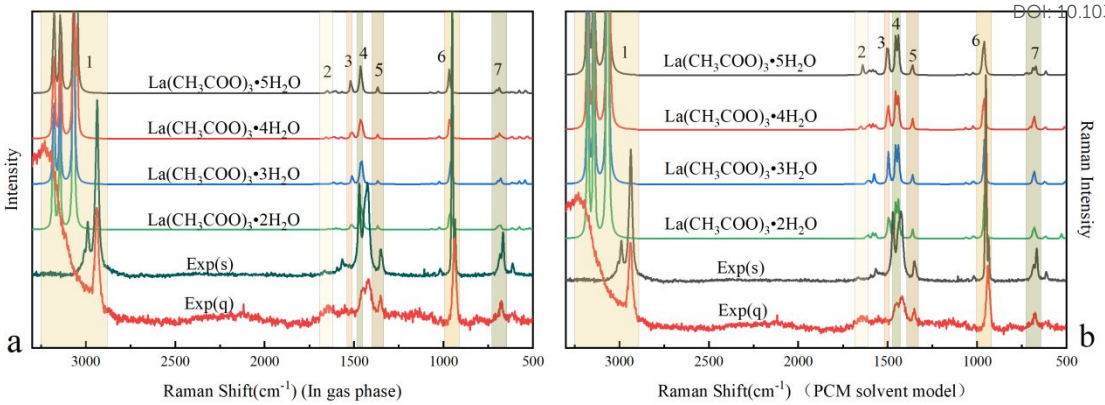

Figure 3 Comparison of experimental and theoretical Raman spectra of lanthanum acetate clusters (a) Theoretical and experimental Raman spectra in gas phase (b) Theoretical and experimental Raman spectra in PCM

3.4 Surface electrostatic potential of clusters

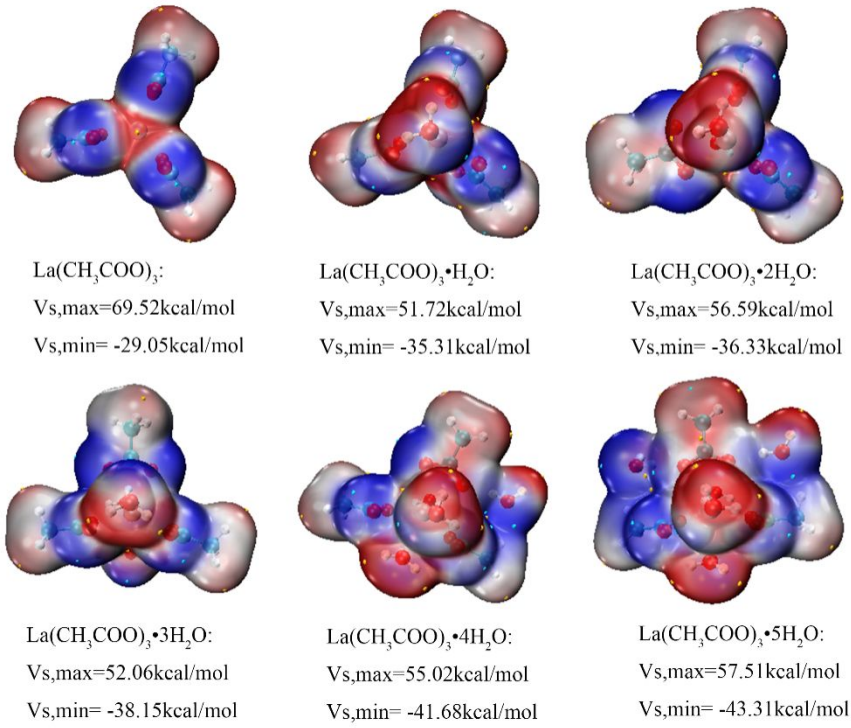

Figure 4 Distribution of electrostatic potential on the surface of lanthanum acetate clusters

Figure 4 presents the ESP distribution of the six clusters of $La(CH_3COO)_3 \cdot nH_2O$ (n=0~5). The red indicates regions of positive potential, while blue indicates the region of negative potential. As shown in **Figure 4**, lanthanum, the hydrogen atoms in water and the methyl groups

in acetate exhibit positive electrostatic potential, while the oxygen atoms in water and the carboxyl groups in acetate exhibit negative electrostatic potential. As the number of water molecules increases, the maximum electrostatic potential of lanthanum acetate hydrated clusters fluctuates between 51.72 and 69.52 kcal/mol, while the minimum value decreased rapidly.

Table 1 presents the interaction properties of $La(CH_3COO)_3 \bullet nH_2O$ (n=0~5) clusters based on their surface ESP distribution. The data in Table 1 show that as the number of water molecules increases, the total variance of the ESP, the variance of the positive and negative portions in the lanthanum acetate hydrated clusters also increases. This suggests that with more water molecules, the clusters are more likely to interact with other molecules through the electrostatic interaction. This trend is further supported by comparing the variance values of the saturated clusters in both the gas phase and the PCM model. Among the clusters in the gas phase, all except $La(CH_3COO)_3 \bullet H_2O$ have σ_+^2 values greater than σ_-^2, indicating that they are more likely to interact with other molecules through their positive electrostatic potential regions. As the number of water molecules increases, the $\nu\sigma_{tot}^2$ value in the cluster gradually rises, with the $La(CH_3COO)_3 \bullet 3H_2O$ cluster in the PCM model exhibiting the highest $\nu\sigma_{tot}^2$ value. A high $\nu\sigma_{tot}^2$ value suggests that the molecule has strong and well-distributed electrostatic potential regions, making it more likely to engage in electrostatic interactions with other molecules, such as water.

Table 1 Surface electrostatic potential analysis

Cluster	Π (kcal/mol)	σ_{tot}^2 (kcal/mol)^2	σ_+^2 (kcal/mol)^2	σ_-^2 (kcal/mol)^2	ν	$\nu\sigma_{tot}^2$ (kcal/mol)^2
$La(CH_3COO)_3$	13.08	175.79	102.88	72.91	0.2427	42.66
$La(CH_3COO)_3 \bullet H_2O$	12.73	177.55	80.96	96.59	0.2481	44.05
$La(CH_3COO)_3 \bullet 2H_2O$	12.52	194.12	102.13	91.99	0.2493	48.39
$La(CH_3COO)_3 \bullet 3H_2O$	12.59	213.62	116.40	97.22	0.2480	52.98
$La(CH_3COO)_3 \bullet 4H_2O$	13.41	223.88	130.12	93.76	0.2434	54.49
$La(CH_3COO)_3 \bullet 5H_2O$	14.27	249.48	147.46	102.02	0.2417	60.30
$La(CH_3COO)_3 \bullet 3H_2O$(PCM)	15.19	328.58	157.23	171.35	0.2495	81.98

3.5 The distribution and localization of electron density in clusters

Figure 5(a) presents the LOL color map on the O_{AC}-La-O_{AC} plane of the $La(CH_3COO)_3 \bullet 5H_2O$ cluster, with values ranging from 0 to 1. High LOL values indicate regions of significant electron localization, typically corresponding to bonding regions, lone pairs, or core orbitals. In

Figure 5(a), areas of higher LOL value are observed between the C-O and C-C atoms in the acetate ion, highlighting notable electron localization. The lone-pair electron regions on the two oxygen atoms of the acetate group also exhibit significant electron localization (red regions). In the direction of the lone pairs, regions of medium electron localization (green regions) extend towards the lanthanum ion and connect with the large orbital of the lanthanum ion.

Figure 5(b) illustrates the electron density difference for the $La(CH_3COO)_3 \cdot 5H_2O$ cluster. In the electron density difference isosurface plots, green and blue colors represent isosurfaces with differences of 0.001 and -0.001, respectively, highlighting the main regions of electron density increase and decrease. Following the formation of the lanthanum acetate hydrated cluster, as shown in **Figure 5**(b), the electron density around the peripheral atoms (water molecules, carboxyl groups, and hydrogen atoms in the methyl group) decreases, while it increases at the center of the cluster (between La and O atoms in the acetate and water molecules). Additionally, charge transfer occurs from the hydrogen atoms in the methyl group to the attached carbon results in an increase in electron density around the carbon. This indicates that the interaction within the hydrated lanthanum acetate cluster is characterized by electron transfer, which lowers the overall energy of the cluster and stabilizes its structure.

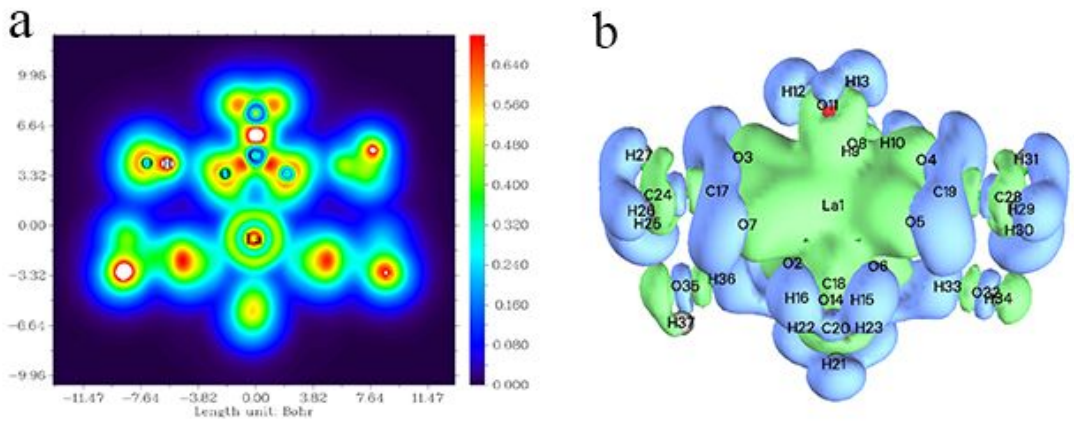

Figure 5 The localized orbital locator (LOL) (a) and the electron density difference (b) of the $La(CH_3COO)_3$-$5H_2O$ cluster.

3.6 Topology analysis for the electron density of hydrated clusters

Figure 6 shows the electron density topology of six clusters of $La(CH_3COO)_3 \cdot nH_2O$ (n=0~5). The figure reveals bond critical points and bond paths between the rare earth ions and both water molecules and acetate ions, as well as between the acetate ions and water molecules. This

indicates that the interaction between acetate and water during clusters formation contributes to the overall structural stability of the clusters.

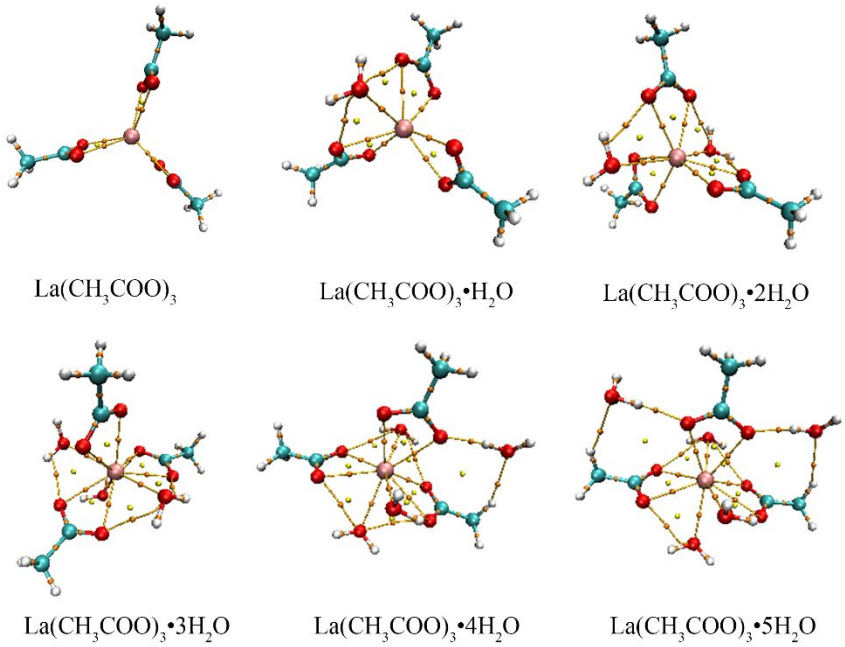

Figure 6 Topology and bond critical point distribution of hydrated clusters

Table 2 Average electron density (ρ), Laplace value of average electron density ($\nabla^2\rho$) and average electron energy density (H)/a.u. for the critical point of rare earth hydrated cluster bond.

cluster	BCP	ρ	$\nabla^2\rho$	H
$La(CH_3COO)_3$	La-O(CH_3COO)	0.05803	0.18357	-0.00506
$La(CH_3COO)_3•H_2O$	La-O(CH_3COO)	0.05378	0.17182	-0.00375
	La-O(H_2O)	0.03872	0.13840	0.00089
$La(CH_3COO)_3•2H_2O$	La-O(CH_3COO)	0.05034	0.16256	-0.00274
	La-O(H_2O)	0.03603	0.13266	0.00148
$La(CH_3COO)_3•3H_2O$	La-O(CH_3COO)	0.04681	0.15204	-0.00185
	La-O(H_2O)	0.03528	0.12831	0.00142
$La(CH_3COO)_3•4H_2O$	La-O(CH_3COO)	0.04672	0.15238	-0.00177
	La-O(H_2O)	0.02718	0.10001	0.00126
$La(CH_3COO)_3•5H_2O$	La-O(CH_3COO)	0.04688	0.15354	-0.00175
	La-O(H_2O)	0.02220	0.08258	0.00116
$La(CH_3COO)_3•3H_2O$(PCM)	La-O(CH_3COO)	0.04338	0.14069	-0.00107
	La-O(H_2O)	0.03376	0.12176	0.00156

Table 2 lists the average electron density (ρ), the Laplace value of the average electron density ($\nabla^2\rho$) and the average electron energy density (H) at the bond critical point between the rare earth ion and the ligands in the lanthanum acetate cluster. The data show that the ρ value for the lanthanum ion's interaction with acetate in the hydrated lanthanum acetate cluster is greater than that for its interaction with water molecules, indicating a stronger interaction between

lanthanum and acetate compared to lanthanum and water molecules. As the number of water molecules increases, the ρ value for lanthanum with both water molecules and acetate decreases, suggesting a weakening of the interaction between lanthanum and both water molecules and acetate. Additionally, the ρ value of saturated clusters in the presence of solvent decreases compared to that in the gas phase, further indicating that water molecules weaken the interaction between lanthanum ions and acetate. The Laplace value ($\nabla^2\rho$) between the lanthanum ions and ligands are all greater than zero, indicating that the interactions between lanthanum ions and acetate and water molecules are closed-shell layer interactions. This suggests that the lanthanum ions primarily engage in ionic bond and van der Waals interactions with ligands. The H value between lanthanum and acetate is less than zero, indicating a partial covalent interaction, likely due to the partial transfer of electrons from acetate into the lanthanum orbitals. As a result, the coordination bond between lanthanum and the oxygen in acetate ion is more stable than that between lanthanum ion and water.

3.7 Noncovalent interaction in the hydrated clusters

Figure 7 presents the RDG scatter plots and color-filled isosurface plots for the six $La(CH_3COO)_3 \cdot nH_2O$ (n=0~5) clusters. The plots reveal that the interaction regions between lanthanum and acetate, or between lanthanum and the water molecules in the first hydration layer, are generally blue, indicating stronger interactions. In contrast, the interaction regions between water and acetate are primarily green with some red, suggesting hydrogen bonding with spatial hindrance. From the scatter plots in the figure, it is evident that the lanthanum acetate hydrated cluster exhibits more spikes than the anhydrous lanthanum acetate cluster, indicating a greater number of interaction sites in the hydrated cluster. Combined with the isosurface plots, it can be observed that a weaker hydrogen bond is formed between the hydrogen atoms in the water and the oxygen atom in the acetate in the second hydration layer.

View Article Online
DOI: 10.1039/D5NJ01601K

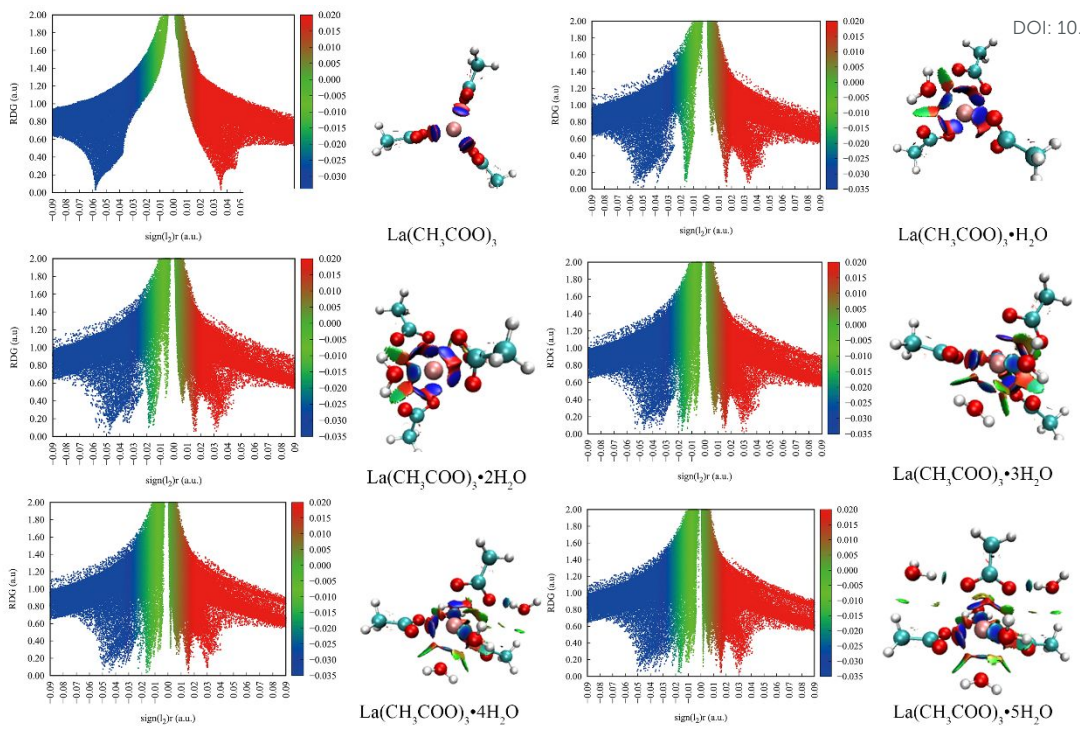

Figure 7 Sign[λ(r)]ρ(r)-RDG scatter plot and RDG equivalent surface plot of lanthanum acetate cluster (RDG = 0.5 a.u.) (scatter plot on the left, equivalent surface plot on the right)

3.8 Binding and Hydration Energies of Lanthanum Acetate Hydrated Clusters

Figure 8 presents the binding energies of $La(CH_3COO)_3 \cdot nH_2O$ (n=0~5) clusters in the gas phase and $La(CH_3COO)_3 \cdot nH_2O$ (n=2~5) clusters in the PCM solvent model. It can be seen that ΔE is slightly less than ΔG for the same clusters. Additionally, ΔE for the lanthanum acetate cluster decreases as the number of water molecules increases, while ΔG reaches its minimum for the $La(CH_3COO)_3 \cdot 3H_2O$ cluster, indicating that $La(CH_3COO)_3 \cdot 3H_2O$ is the most stable. This finding corroborates the earlier conclusion that the first hydration layer of the lanthanum acetate cluster becomes saturated with three water molecules. Comparing the binding energies of the clusters in the gas phase and in the solvent reveals that the binding energy is lower in the PCM solvent model than in the gas phase, due to the influence of the solvent.

View Article Online
DOI: 10.1039/D5NJ01601K

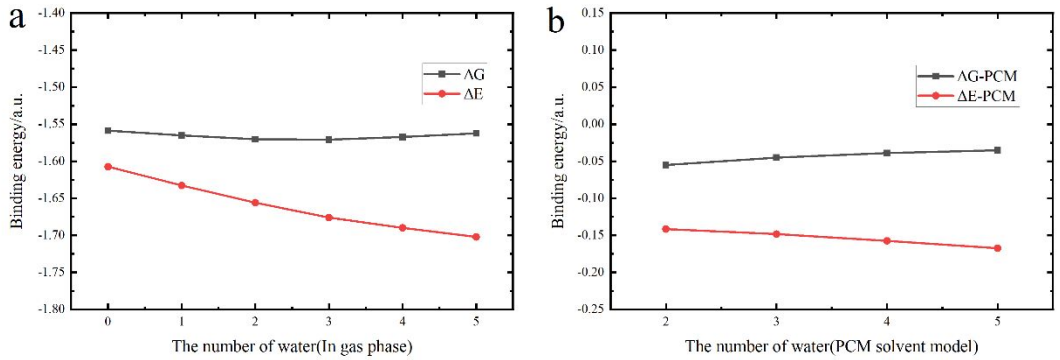

Figure 8 Binding energy of lanthanum acetate clusters/a.u. (a) ΔE and ΔG for gas phase clusters; (b) ΔE and ΔG in PCM

Table 3 lists the binding energies and hydration energies of the lanthanum acetate clusters. where a larger absolute value (more negative) indicates stronger interparticle cohesion. The data show that in both gas-phase and aqueous environments, the binding energy of copper acetate clusters follows a consistent trend: as the hydration number (number of crystalline water molecules) increases from 2 to 5, $\Delta E_{binding}$ becomes more negative (larger in magnitude), demonstrating that higher hydration leads to tighter particle binding within the clusters. However, the absolute values of $\Delta E_{binding}$ in the aqueous phase are significantly smaller than those in the gas phase. This is because solvent water molecules in the aqueous environment interact with the cluster particles, weakening the intrinsic binding energy within the clusters. Additionally, $\Delta G_{hydration}$ reflects the Gibbs free energy change during the hydration process of the clusters. Its values fluctuate overall but become notably more negative at a hydration number of 5, indicating that stronger hydration (e.g., 5-water coordination) leads to more pronounced adjustments (increases) in binding energy. This reveals a synergistic relationship between hydration effects and binding energy in stabilizing the cluster structure.

Table 3 The binding and hydration energies of lanthanum acetate hydrated clusters （kcal/mol）

Claster	In gas phase		In water		$\Delta G_{hydration}$
	$\Delta G_{binding}$	$\Delta E_{binding}$	$\Delta G_{binding}$	$\Delta E_{binding}$	
$La(CH_3COO)_3 \cdot 2H_2O$	-985.3	-1039.0	-34.5	-88.7	-19.7
$La(CH_3COO)_3 \cdot 3H_2O$	-985.6	-1051.7	-28.3	-93.0	-18.2
$La(CH_3COO)_3 \cdot 4H_2O$	-983.4	-1060.4	-24.4	-98.7	-21.6
$La(CH_3COO)_3 \cdot 5H_2O$	-980.3	-1068.0	-22.0	-105.0	-27.4

3.9 Variations of RDF and CN with temperature in MD simulation of lanthanum acetate solution

Figure 9a and 9b presents the RDF and coordination number of La with oxygen atoms in the ligands at various temperatures. The La-O(ac^-) RDF peaks appear between 0.21-0.23 nm, while the La-O(H_2O) peak occur between 0.23-0.25 nm. The significantly higher peak intensity of the La-O(ac^-) compared to La-O(H_2O) indicates much stronger interactions between La^{3+} and acetate ions (ac^-) than between La^{3+} and water molecules. This phenomenon demonstrates that acetate ions form more stable coordination bonds with La^{3+}. Within a specific distance from La^{3+}, oxygen atoms from acetate ions exhibit substantially higher distribution density than those from water molecules, displaying more regular local ordering. In the coordination competition, acetate ions show clear preferential binding to La^{3+} over water molecules. This preference arises because the electrostatic interaction between acetate ions and La^{3+} exceeds the solvation interaction between water molecules and La^{3+}, creating a more stable and ordered local ionic environment. These results agree with previous quantitative findings[37].

The data reveal that increasing temperature enhances the RDF peak intensity and coordination number for La-O(ac^-), while reducing those for La-O(H_2O). This temperature-dependent behavior reflects dynamic reorganization of La^{3+} coordination structures and thermal effects on competitive coordination. The trend suggests that at elevated temperatures, more acetate ions coordinate with lanthanum while fewer water molecules remain in the coordination shell, leading to increased lanthanum acetate aggregation. This aligns with the experimentally observed decrease in the solubility of lanthanum acetate at elevated temperatures.

Notably, the combined coordination numbers of La-O(ac^-) and La-O(H_2O) consistently total approximately 9 across conditions, matching previous reports that lanthanide complexes achieve coordination saturation at this number[38]. Additionally, rising temperature causes a slightly outward shifts in the La-O(ac^-) RDF peak position from 0.218 nm to 0.220 nm, indicating increased La-acetate distances. This shift likely results from progressive conversion of acetate coordination from monodentate to bidentate as more acetate ions bind to La^{3+}.

The RDF peak shifts (La-O(ac^-) moving from 0.218 nm at 275 K to 0.220 nm at 325 K) reflect temperature-induced expansion of La-acetate distances, attributable to thermal expansion and enhanced molecular motion. Concurrently, the CN for La-O(ac^-) increases from ~6 to ~7, indicating more acetate ions coordinate with La^{3+} despite the larger distance, likely due to weakened hydration shells at higher temperatures.

View Article Online
DOI: 10.1039/D5NJ01601K

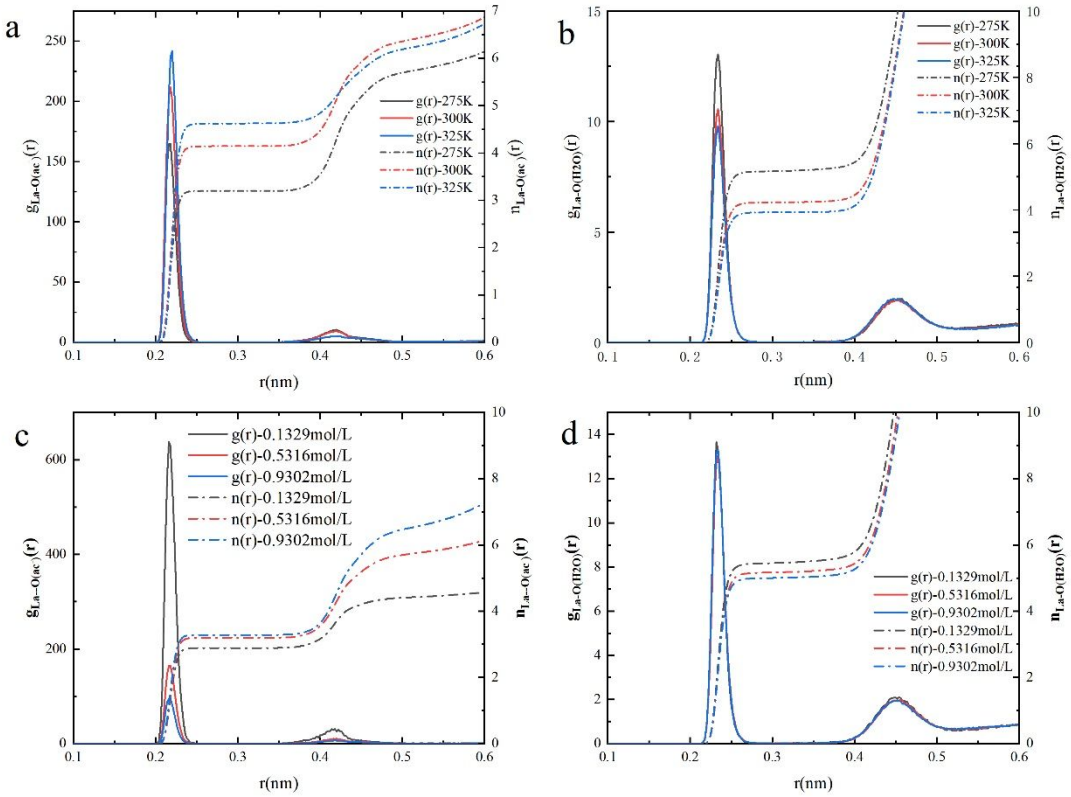

Figure 9 Radial distribution function (RDFs, g(r)) and coordination number (CNs) of La-O(ac^-) and La-O(H_2O) in lanthanum acetate solution at different temperatures and temperatures simulated by MD n(r)) (a) La-O(ac^-) at different temperatures (b) La-O(H_2O) at different temperatures (c) La-O(ac^-) at different concentrations (d) La-O(H_2O) at different concentrations

To correlate structural changes with energetics, we calculated the binding free energy (ΔG) of $La(CH_3COO)_3 \bullet nH_2O$ clusters at different temperatures using the PCM model (Table 4). The data in Table 4 reveal that the binding free energy (ΔG) of the clusters becomes less negative with increasing temperature, rising from -32.4 kcal/mol to -23.4 kcal/mol, indicating decreasing stability at higher temperatures. This trend is primarily driven by entropic effects: while the enthalpy change (ΔH) remains negative throughout (-82.9 to -81.9 kcal/mol), demonstrating an exothermic binding process, its contribution shows only minor variations. In contrast, the significantly negative entropy change (ΔS) (-183.3 to -180.0 cal/mol·K) reveals that cluster formation increases system ordering, resulting in a substantial entropy penalty.

As temperature increases, the entropy penalty term (-TΔS) grows from 50.6 cal/mol at 275 K to 58.5 cal/mol at 325 K, overwhelmingly surpassing the modest enthalpy adjustment and

becoming the dominant factor in ΔG destabilization. Although the negative ΔS value shows a slight decrease at higher temperatures (possibly due to enhanced coordination flexibility or solvent disorder), this reduction is insufficient to counteract the amplified entropy penalty caused by rising temperature. These results demonstrate that the thermal instability of the clusters primarily stems from the strengthening entropy-reducing constraints.

Table 4 Thermodynamic Data of $La(CH_3COO)_3 \cdot 3H_2O$ clusters in PCM model at Different Temperatures

T (K)	275	300	325
ΔG (kcal/mol)	-32.4	-27.9	-23.4
ΔH (kcal/mol)	-82.9	-82.4	-81.9
-TΔS (cal/mol)	50.6	54.5	58.5
ΔS (cal/mol·K)	-183.3	-181.6	-180.0

3.10 Variations of RDF and CN with concentration in MD simulation of lanthanum acetate solution

Figure 9c and 9d present the RDF and CN of La with oxygen in the ligands at different concentrations. The data reveal that the peak intensity of the La-O(ac^-) RDF decreases with increasing ion concentration, while its coordination number shows a slight increase. Conversely, the peak intensity of the La-O(H_2O) RDF remains relatively unchanged, with a minor decrease in coordination number. The position of the first solvation shell peak remains consistent across concentrations, indicating stable nearest-neighbor distances. The possible reasons for analysis could be that larger interionic distances and weaker shielding by solvent water allow La^{3+} and acetate ions to form locally ordered structures (e.g., ion pairs or solvation shells) at low concentrations, resulting in pronounced RDF peaks at specific distances. At high concentrations, reduced interionic spacing and competitive interactions among numerous ions and solvent molecules disrupt long-range ordering, leading to diminished RDF peak intensities or even flattened profiles. The Debye screening length of the ionic atmosphere shortens, more effectively screening electrostatic interactions between ions and weakening their correlations—manifested as reduced RDF peaks. Furthermore, high concentrations may destabilize the solvation shells of ions (e.g., disrupting the ordered arrangement of water molecules), increasing the probability of direct ion-ion contact while reducing overall correlation (evidenced by the lowered first peak in the RDF).

View Article Online
DOI: 10.1039/D5NJ01601K

3.11 aNCI analysis

During the molecular dynamics simulations, the average non-covalent interaction (aNCI) and thermal fluctuation index (TFI) plots for lanthanum (La) and ligand ions are shown in **Figure 10**. In aNCI analysis, blue regions typically correspond to strong attractive non-covalent interactions, indicating significant binding forces between the La^{3+} and the acetate ions/water molecules. These interactions facilitate them to approach each other and form stable structures. On the other hand, red generally denotes steric hindrance, suggesting that the spatial arrangement of acetate groups and water molecules around the La^{3+} ion leads to steric repulsion due to their structural bulk and mutual positioning. However, this steric effect does not disrupt the overall interactions. Rather, it indirectly confirms that the particles have approached each other closely enough to induce spatial crowding.

In the TFI plot, the spatial regions between the central lanthanum ion and acetate groups/water molecules are displayed in blue and green respectively, demonstrating the thermal stability of these interactions.. This means that even under the thermally fluctuating conditions of molecular dynamics simulations—where system particles are in constant motion and energy levels fluctuate—the interactions between the lanthanum ion and these two types of ligands persist without being easily disrupted or significantly altered by thermal motion. This observation reflects the formation of relatively stable interactions between lanthanum and acetate, as well as between lanthanum and water molecules. Such stable interactions serve as a crucial foundation for maintaining the structure of lanthanum acetate hydrated clusters and influencing their thermodynamic properties, such as binding energy and hydration behavior.

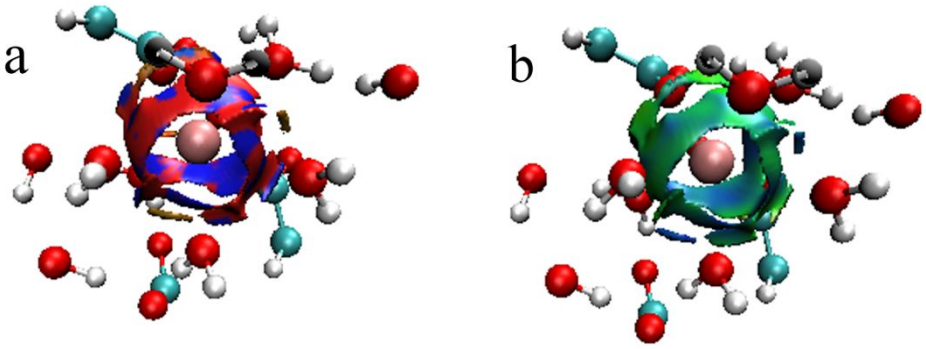

Figure 10 aNCI (a) and TFI (b) diagrams of La and ligand ions during MD simulation

View Article Online
DOI: 10.1039/D5NJ01601K

4 Conclusions

The lanthanum acetate hydrate clusters exhibit a coordination number of approximately 9, consistent with previous findings that lanthanum complexes reach saturation at this coordination number. The binding energy of the $La(CH_3COO)_3 \bullet 3H_2O$ cluster is the lowest, indicating its stability. The first hydration layer of the lanthanum acetate cluster reaches saturation when the number of water molecules is 3. The lanthanum ion forms strong interactions with both acetate and water molecules, with acetate ligands coordinating through oxygen atoms and stabilizing the structure through electrostatic and steric interactions. The water molecules contribute to the hydration shell, further enhancing the stability of the complex.

As the concentration of lanthanum acetate increases, the aggregation of clusters also increases, as indicated by changes in the radial distribution function (RDF) and coordination numbers. The aNCI and TFI diagrams reveal that lanthanum, acetate, and water molecules are strongly interacting, with steric hindrance present in the system. These interactions are primarily governed by electrostatic forces, with steric effects playing a significant role in the overall stability of the clusters. These findings offer valuable insights into the influence of organic ammonium leaching agents on the structure and the evolution of rare earth hydrated clusters at the microscopic level.

Acknowledgment

This work was financially supported by the National Natural Science Foundation of China under Contract Number (52174257) and supported by the Graduate Innovative Fund of Wuhan Institute of Technology (No. CX2024016). The numerical calculations in this paper have been done on the supercomputing system in the Supercomputing Center of Wuhan University.

References

[1] V. Balaram, in: A. Anbar, D. Weis (Eds.), Treatise on Geochemistry (Third edition), Elsevier, Oxford, 2025, p. 193-233.

[2] Z. Liao, Z. Yuan, H. Gao, F. Meng, Doped rare earth elements enhance gas sensing properties of hollow spiral-like Mn(OH)F semiconductor sensors for acetate esters detection. *Sensors and Actuators B: Chemical* **2024,** *412*, 135825.

[3] J. Tian, X. Tang, J. Yin, X. Luo, G. Rao, M. Jiang, Process optimization on leaching of a lean weathered crust elution-deposited rare earth ores. *Int J Miner Process* **2013,** *119*, 83.

[4] C. Wang, L. Wang, L. Li, T. Wei, J.-J. Huang, Y. Yang, Experiments on Leaching of Different Grades of ion type rare earth ores with (NH4)2SO4/MgSO4. *Chinese Rare Earths* **2018,** *39* (1), 67.

[5] Z. He, Z. Zhang, J. Yu, Z. Xu, R.a. Chi, Process optimization of rare earth and aluminum leaching from weathered crust elution-deposited rare earth ore with compound ammonium salts. *J Rare Earth* **2016,** *34* (4), 413.

[6] Y. Xu, G. Wang, J. Xu, S. Kang, J. Zhu, X. Liang, Y. Yang, J. Wei, H. He, Recovery of rare earth elements from ion-adsorption deposits using electro kinetic technology: A comparative study on leaching agents. *Chem Eng J* **2024,** *499*, 156094.

[7] H. Yan, T. Liang, Q. Liu, T. Qiu, G. Ai, Compound leaching behavior and regularity of ionic rare earth ore. *Powder Technol* **2018,** *333*, 106.

[8] J. Feng, X. Wu, Z. Gao, W. Sun, F. Zhou, R. Chi, Leaching Behavior of Rare Earth Elements and Aluminum from Weathered Crust Elution-Deposited Rare Earth Ore with Ammonium Formate Inhibitor. *Minerals* **2023,** *13* (10), 1245.

[9] W. Chen, Z. Zhang, R.a. Chi, Assisted Leaching Process of Weathered Crust Elution-Deposited Rare Earth Ore by Ammonium Carboxylate. *J Metal Mine* **2020,** (5), 191.

[10] X.-Y. Yue, Y.-Y. Li, Q.-W. Zhang, G. Liao, H.-B. Yi, Synergistic effects of hydration shells and ion association on Li+ selectivity of bivalent cations adsorbed carboxylate graphene nanopore: A molecular simulation study. *J Mol Liq* **2021,** *327*, 114877.

[11] M. Wang, C.-C. Wang, H.-Q. Cai, Y.-Y. Li, Q.-W. Zhang, H.-B. Yi, Molecular dynamics simulation study on distinctive hydration characteristics of highly coordinated calcium chloride complexes. *J Mol Liq* **2019,** *274*, 261.

[12] C.-C. Wang, M. Wang, H.-Q. Cai, Q.-W. Zhang, Y.-Y. Li, H.-B. Yi, Insight into the roles of two typical ion clusters and their second hydration shells: Implication for the nucleation mechanism in MgSO4 aqueous solution. *J Mol Liq* **2019,** *278*, 33.

[13] M.F.J. Mabesoone, A.R.A. Palmans, E.W. Meijer, Solute-Solvent Interactions in Modern Physical Organic Chemistry: Supramolecular Polymers as a Muse. *J Am Chem Soc* **2020,** *142* (47), 19781.

[14] Z. Zou, L. Huang, X. Li, J. Xu, X. Zeng, R. Shu, B. Xiao, J. Ou, W. Huang, Adsorption of Hydrated Pr3+ and NH4+/Mg2+ Ions onto the (001) Surface of Montmorillonite: A DFT Analysis with Experimental Verification. *Minerals* **2022,** *12* (11).

[15] M.J. Frisch, G.W. Trucks, H.B. Schlegel, G.E. Scuseria, M.A. Robb, J.R. Cheeseman, G. Scalmani, V. Barone, G.A. Petersson, H. Nakatsuji, X. Li, M. Caricato, A.V. Marenich, J. Bloino, B.G. Janesko, R. Gomperts, B. Mennucci, H.P. Hratchian, J.V. Ortiz, A.F. Izmaylov, J.L. Sonnenberg, Williams, F. Ding, F. Lipparini, F. Egidi, J. Goings, B. Peng, A. Petrone, T. Henderson, D. Ranasinghe, V.G. Zakrzewski, J. Gao, N. Rega, G. Zheng, W. Liang, M. Hada, M. Ehara, K. Toyota, R. Fukuda, J. Hasegawa, M. Ishida, T. Nakajima, Y. Honda, O. Kitao, H. Nakai, T. Vreven, K. Throssell, J.A. Montgomery Jr., J.E. Peralta, F. Ogliaro, M.J. Bearpark, J.J. Heyd, E.N. Brothers, K.N. Kudin, V.N. Staroverov, T.A. Keith, R. Kobayashi, J. Normand, K. Raghavachari, A.P. Rendell, J.C. Burant, S.S. Iyengar, J. Tomasi, M. Cossi, J.M. Millam, M. Klene, C. Adamo, R. Cammi, J.W. Ochterski, R.L. Martin, K. Morokuma, O. Farkas, J.B. Foresman, D.J. Fox, Wallingford, CT, 2016.

[16] B. Mennucci, J. Tomasi, R. Cammi, J.R. Cheeseman, M.J. Frisch, F.J. Devlin, S. Gabriel, P.J. Stephens, Polarizable Continuum Model (PCM) Calculations of Solvent Effects on Optical Rotations of Chiral Molecules. *The Journal of Physical Chemistry A* **2002,** *106* (25), 6102.

[17] J.S. Murray, T. Brinck, P. Lane, K. Paulsen, P. Politzer, Statistically-based interaction indices derived from molecular surface electrostatic potentials: a general interaction properties function (GIPF). *Journal of Molecular Structure: THEOCHEM* **1994,** *307*, 55.

[18] M.D. Driver, M.J. Williamson, J.L. Cook, C.A. Hunter, Functional group interaction profiles: a general treatment of solvent effects on non-covalent interactions. *Chemical Science* **2020,** *11* (17), 4456.

[19] A.V. Afonin, V.A. Semenov, A.V. Vashchenko, Localized orbital locator as a descriptor for quantification and digital presentation of lone pairs: benchmark calculations of 4-substituted pyridines. *Phys Chem Chem Phys* **2021,** *23* (43), 24536.

[20] A.D. Becke, K.E. Edgecombe, A simple measure of electron localization in atomic and molecular systems. *The Journal of Chemical Physics* **1990,** *92* (9), 5397.

[21] J.F. Harrison, On the role of the electron density difference in the interpretation of molecular properties. *The Journal of Chemical Physics* **2003,** *119* (16), 8763.

[22] M.C. Burla, B. Carrozzini, G.L. Cascarano, C. Giacovazzo, G. Polidori, About difference electron densities and their properties. *Acta Crystallogr A* **2017,** *73* (6), 460.

[23] R.F. Nalewajski, R.G. Parr, Information theory, atoms in molecules, and molecular similarity. **2000,** *97* (16), 8879.

[24] P.S.V. Kumar, V. Raghavendra, V. Subramanian, Bader's Theory of Atoms in Molecules (AIM) and its Applications to Chemical Bonding. *Journal of Chemical Sciences* **2016,** *128* (10), 1527.

[25] D. Morales-Pumarino, J.E. Barquera-Lozada, Electron density and its reduced density gradient in the study of π–π interactions. **2023,** *123* (18), e27051.

[26] M. Tahenti, N. Issaoui, T. Roisnel, H. Marouani, Synthesis, characterization, and computational survey of a novel material template o-xylylenediamine. *Journal of the Iranian Chemical Society* **2021**.

[27] C. Fan, Y. Liu, S. Tarik, X. Cao, A Theoretical Study on Terpene-Based Natural Deep Eutectic Solvent: Relationship between Viscosity and Hydrogen-Bonding Interactions. *Global Challenges* **2021,** *5*, 2000103.

[28] P. Wu, R. Chaudret, X. Hu, W. Yang, Noncovalent Interaction Analysis in Fluctuating Environments. *Journal of chemical theory and computation* **2013,** *9* (5), 2226.

[29] T. Lu, F. Chen, Multiwfn: A multifunctional wavefunction analyzer. *J Comput Chem* **2012,** *33* (5), 580.

[30] W. Humphrey, A. Dalke, K. Schulten, VMD: Visual molecular dynamics. *Journal of Molecular Graphics* **1996,** *14* (1), 33.

[31] X. Li, Y. Zhang, L. Zou, M. Zhang, R. Chi, A density functional theory (DFT) on the leaching process of weathered crust elution-deposited rare earth ore with lixiviants. *Miner Eng* **2023,** *191*, 107980.

[32] T. Lu, Sobtop Version [1.0(dev3.1)]. *http://sobereva.com/soft/Sobtop* **2022**.

[33] M. Abraham, A. Alekseenko, V. Basov, C. Bergh, E. Briand, A. Brown, M. Doijade, G. Fiorin, S. Fleischmann, S. Gorelov, G. Gouaillardet, A. Grey, M.E. Irrgang, F. Jalalypour, J. Jordan, C. Kutzner, J.A. Lemkul, M. Lundborg, P. Merz, E. Lindahl, GROMACS 2024.4 Manual (2024.4). Zenodo, 2024.

[34] A.B. Marahatta, Applications of Radial Distribution Function (RDFg(r)) Tool in Statistical Analyses of Microcanonical Ensembles. *International Journal of Progressive Sciences and Technologies* **2024,** *44* (1), 150.

[35] X. Chen, T.-T. Chen, W.-L. Li, J.-B. Lu, L.-J. Zhao, T. Jian, H.-S. Hu, L.-S. Wang, J. Li, Lanthanides with Unusually Low Oxidation States in the PrB3– and PrB4– Boride Clusters. *Inorg Chem* **2019,** *58* (1), 411.

[36] W.W. Rudolph, G. Irmer, A Raman Spectroscopic Study of Aqueous La(CH3CO2)3 Solutions and La(CH3CO2)3·1.5 H2O(cr). *J Solut Chem* **2017,** *46* (1), 190.

[37] X. Chai, G. Li, Z. Zhang, R. Chi, Z. Chen, Leaching Kinetics of Weathered Crust Elution-Deposited Rare Earth Ore with Compound Ammonium Carboxylate. *Minerals* **2020,** *10* (6).

[38] J. Legendziewicz, Structure and Spectroscopy of Selected Lanthanide Compounds with Coordination Number from 9 to 6. *Acta Phys Pol A* **1996,** *90* (1), 127.

View Article Online
DOI: 10.1039/D5NJ01601K

Data Availability Statement

All experimental and computational data associated with this article are included in the main text or the electronic supplementary information (ESI).